



Developing a High-Strength Al–Mg–Si Alloy with Improved Electrical Conductivity by a Novel ECAP Route

Nannan Zhao^{1,2} · Chunyan Ban^{1,2}

Received: 6 September 2021 / Accepted: 9 December 2021 / Published online: 22 April 2022
© The Korean Institute of Metals and Materials 2022

Abstract

This paper investigated the microstructure, tensile and electrical properties of an equal channel angular pressed 6063 Al alloy at temperatures ranging from room temperature (RT) to 300 °C. Additionally, a two-step temperature schedule (TST) was applied to improve the combined property of the low-alloyed Al–Mg–Si alloy. The results suggested that only processing at RT and TST led to a reduction of the grain size and an increase of strength with increasing number of passes, whereas four-pass processing at TST condition produced a better grain refinement and higher strength compared to the RT counterpart. Detailed analysis reveals that apart from the grain refinement, high-density dislocations and formation of nanoscale precipitates play the dominant roles in strengthening. These microstructural features provide the four-pass TST sample exceptional increase in strength about 67 MPa compared to RT counterpart. Besides, precipitation of solutes in form of numerous nanoscale precipitates can purify the Al matrix in the TST samples, resulting in the improved electrical conductivity as compared to RT sample. The TST method as a new strategy can improve strength and electrical conductivity by controlling the nanosized precipitates in an ultrafine-grained structure, which indeed provides an opportunity for low-alloyed Al–Mg–Si alloys to obtain the better combination properties.

Keywords Equal channel angular pressing · Aluminum alloy · Strength · Electrical conductivity

1 Introduction

Severe plastic deformation (SPD) techniques, such as high-pressure torsion (HPT) and equal channel angular pressing (ECAP), are effective methods to refine grain sizes down to sub-micrometer or even nanometer level [1]. As expected from Hall–Petch relationship, the ultrafine-grained (UFG) microstructure induced by SPD method results in a high strength in a number of pure metals and alloys [2, 3], including heat treatable aluminum alloys. These aluminum alloys can attain superior strength by combination of SPD processing and precipitation [4, 5], simultaneously incorporating grain boundary hardening, strain hardening as well as additional precipitation hardening. In practice, these heat

treatable Al alloys are difficult to process but can be easily processed at elevated temperatures to avoid their premature failure during SPD processes [4, 6]. This could make the SPD processing to have a great commercial potential.

SPD processing temperatures and the level of strains, as the important processing parameters, have effects on the grain refinement and related mechanical properties of the SPD-processed alloys. Generally, when the decomposition of a solid solution is suppressed during SPD processing so that the dilute solutes randomly distribute in the matrix, increasing SPD processing temperature leads to an increase in grain size and a decrease in stress [7, 8]. On the other hands, in the case of decomposition of supersaturated solid solutions during SPD processing, the processing temperature has a complex influence on the grain refinement and mechanical properties due to precipitation and even segregation on grain boundaries [5, 9, 10]. Moreover, SPD processing leads to presence of a high density of dislocation, extremely high concentration of vacancies and large volume fraction of grain boundary. Dynamic interaction of these SPD-induced crystallographic defects with solute atoms can enhance the atoms mobility. Therefore, as processing

✉ Chunyan Ban
bancy@epm.neu.edu.cn

¹ Key Laboratory of Electromagnetic Processing of Materials, Ministry of Education, Northeastern University, Shenyang 110819, China

² School of Materials Science and Engineering, Northeastern University, Shenyang 110819, China

at even low temperature like RT or 110 °C, the formation of precipitates [11, 12], segregation on dislocation cores and grain boundaries [9], and even modified morphology of precipitates [11] and precipitation sequence have been observed in UFG materials. To date, for the age-hardenable aluminum alloys, most previously published researches focused on SPD processing at the isothermal temperature, such as RT or conventional precipitation treatments temperatures (typical 100–200 °C). Thus, the investigation about the effect of SPD processing at a mixed temperature regime on both grain refinement and distribution of the solutes in these alloys is necessary to obtain excellent mechanical properties.

Al–Mg–Si alloys have been widely used in electrical industry due to their high strength-to-weight ratio, good mechanical and electrical properties, formability and corrosion resistance as compared to other Al alloys. In the Al–Mg–Si alloys, the alloying elements can improve the strength through the solution hardening and precipitate hardening. However, these alloying elements may lead to a lower-level electrical conductivity by causing lattice distortion and resulting electron scattering. Strength and electrical conductivity are usually mutually exclusive in most metallic conductive materials. As compared with alloying elements distributed in a random solid solution, grain boundaries can be the less effective in scattering electrons and consequently produce the less negative effect on electrical conductivity [13, 14]. The combine of SPD methods with post-deformation aging treatment have showed high potential to obtain a combination of high strength and high electrical conductivity [8]. However, controlling the precipitation of solute atoms in the resulting UFG structure to produce excellent properties is a challenge because of the concurrent reduction of deformation-induced defects density and grain growth during ageing response, which may lead to a rapid decrease in strength caused by grain growth rather than by a change in the precipitates state [15, 16]. Most recently, it is found that the nanoprecipitates could be the obstacles and sources of dislocations to obtain the high strength and purify the matrix to improves the electrical conductivity [17–19]. Therefore, it should highlight the importance to tailor the nanostructure in UFG Al–Mg–Si alloys through controlling processing parameters in order to produce the age-hardenable alloys with good combination properties.

In the present research, a commercial 6063 Al alloy was processed by ECAP at the isothermal temperatures ranging from RT to 300 °C. The influence of ECAP processing temperatures on the grain refinement, precipitation and properties in the alloy were investigated. To further increase strength of the low-alloyed Al–Mg–Si alloy and achieve a reasonable electrical conductivity at the same time, a two-step processing temperature schedule (TST) as a promising strategy to design the nanoprecipitates in an UFG structure was developed.

2 Experimental Procedures

A commercial 6063 aluminum alloy, having a composition, in wt%, of 0.52 Mg, 0.49Si, 0.09Fe, 0.01 Ti and balance Al, was employed in this study. Rod like billets with 70 mm length and 15 mm diameter cut from the 6063 alloy as-cast ingot for ECAP processing were solution-treated at 560 °C for 1 h, followed by quenching in ice water (referred to as as-annealed state in the rest of the paper). Subsequently, these species were pressed through the ECAP die up to eight passes with Bc route by a rate about 70 mm/min at room temperature (RT), 150 °C, 200 °C and 300 °C, respectively. In addition, the two-step temperature schedule (TST) was carried out: species were processed by two passes at 150 °C, and then followed by pressing at RT up to a total of eight passes, thereafter referred to as TST condition. The ECAP die was combined with two passages crossed at the inner corner angle of 20° and outer corner angle of 90° and the effective strain is about 1.05 once the billet passes through the die one pass. To reduce friction during pressing, the mixture of Molybdenum disulfide and graphite powder were used as the lubricant. The die was packaged with a heating jacket of resistance wires and can be heated to the target temperature. The species were held in the entrance channel for 6 min to attain the temperature before warm ECAP. After each pass processing, species were promptly quenched into water for further passes or characterization. Following the ECAP process, samples processed in RT and TST conditions were aged at 120 °C and 150 °C for up to 24 h to evaluate the aging hardening.

The characteristic microstructures of samples in as-cast and as-annealed state were analyzed using field emission scanning electron microscope (SEM, Zeiss ULTRA 55)) equipped with an energy dispersive X-ray spectroscopy (EDS) attachment. The microstructural change after ECAP processing were characterized using a polarized light microscope (DP74, Olympus). Samples were extracted from center parallel to extrusion direction (ED), and then ground and polished following the standard produce. The samples were etched by a solution of 5 g HFB acid and 200 ml H₂O. Transmission electron microscopy (TEM) and high-resolution TEM (HRTEM) observations were carried out on TECNAL G²20 and JEM-ARM200F microscopes operating at 200 kV to investigate the microstructures of samples processed in different conditions. The element mappings were performed using energy-dispersive X-ray spectroscopy (EDS) to examine the chemical composition of precipitates. Samples for TEM study were cut along extrusion direction, and ground to a thickness of ~ 100 μm. TEM foils were prepared by twin-jet electropolishing with 30% nitric acid in methanol at – 30 °C and with an operating voltage of 25 V.

To evaluate the change of mechanical property of investigated samples, hardness and tensile tests were conducted at room temperature. Vickers hardness was measured on the cross section by a loading of 100 g for 10 s, with each value averaged from 10 readings at least. Tensile tests were carried out at a constant crosshead speed of 0.7 mm/min on an Instron 5969 machine. Yield stress (YS, 0.2% proof stress), ultimate tensile strength (UTS) and total elongation were measured from the engineering stress–strain curves of specific samples with a gauge dimension of $3 \times 2 \times 12.5$ mm and the gauge length parallel to the pressing direction. Electrical conductivity of the alloy at RT was measured on a Sigmascope SMP10 device. Conductivity measurements were performed on the center of longitudinal section. Each sample's surface was grounded by SiC sand-papers and the apparatus calibration with reference samples was conducted at RT prior to measurement. The unit of electrical conductivity is %IACS (International Annealed Copper Standard). X-ray diffraction (XRD) measurements of the ECAPed samples were performed using a Smartlab 9KW diffractometer (Cu K_α). A standard Si was used to determine peak broadening due to instrumental factor. The true peak breadth (B) can be derived from subtracting the instrumental contribution from the observed peak breadth [20], $B = \sqrt{B_{obs}^2 - B_{inst}^2}$, where the B_{obs} and B_{inst} are the observed peak broadening and the instrumental broadening, respectively.

3 Experimental Results

3.1 Tensile Properties of the 6063 Al Alloy Processed by ECAP

The strengths versus the number of passes for as-annealed sample and samples processed at different temperatures ranging from RT up to 300 °C are shown in Fig. 1. After solution treatment, the as-annealed alloy exhibits the very low strength (yield strength about 89 MPa and ultimate strength about 187 MPa). At RT condition, increasing the number of passes provided a gradual improvement of strength. However, the samples processed at 200 °C and 300 °C exhibited a pronounced decrease in strength with increasing in the number of passes. By contrast, for the samples processed at 150 °C, the strength presents a different trend: rise at first, reach the peak point at four passes, and then decrease. After two passes, processing at RT and 200 °C led to a higher yield strength (about 240 MPa) than that of processing at 300 °C (107 MPa), while it is lower than that of processing at 150 °C (268 MPa). With further increasing in the number of passes to eight, an increase of processing temperature provided a significant decrease in strength, excepted for the four-pass ECAP processing at

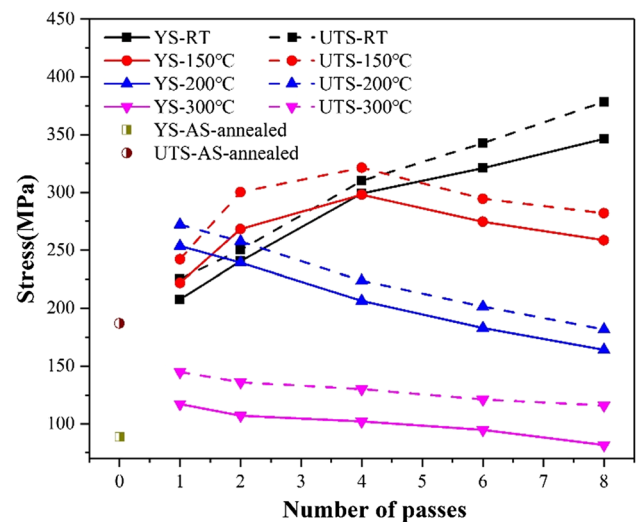


Fig. 1 Strengths of the 6063 Al alloy processed by ECAP at different temperatures

150 °C which led to a yield strength similar to the four-pass ECAP processing at RT. The eight-pass sample processed at RT obtained the highest yield strength of 346 MPa. Obviously, the effect of the processing temperature on strength is significant.

Regarding the TST condition, the representative engineering tensile test stress–strain curves of samples processed by ECAP processing in different conditions are presented in Fig. 2. ECAP processing in TST condition promptly increased strength in comparison with the counterparts processed at homologous temperatures (from RT to 300 °C). Significantly, the four-pass sample processed in TST condition have a yield strength of 366 MPa, which is 67 MPa higher than that of counterpart processed at RT, and even 20 MPa higher than that of eight-pass sample processed in RT condition. After eight passes, processing at TST condition enhanced the ultimate tensile strength up to 400 MPa, which is ~22 MPa higher than that of processing at RT condition. Unlike ECAP processing at 150 °C, ECAP processing at RT and at TST conditions led to the similar trend of strength variation with increasing number of passes. However, ECAP processing from two to four passes at TST condition produced the increase of yield strength about 98 MPa, which is significantly higher than that for every two passes at RT condition (about 55 MPa from two to four passes, thereafter up to eight passes about 26 MPa for every two passes). A summary of tensile properties and electrical conductivity of samples processed at RT and TST condition is given in Table 1. It is noted that for the processing at TST condition there are pronounced increases in combination of strength and electrical conductivity but almost no significantly decrease in ductility as compared to processing at RT condition.

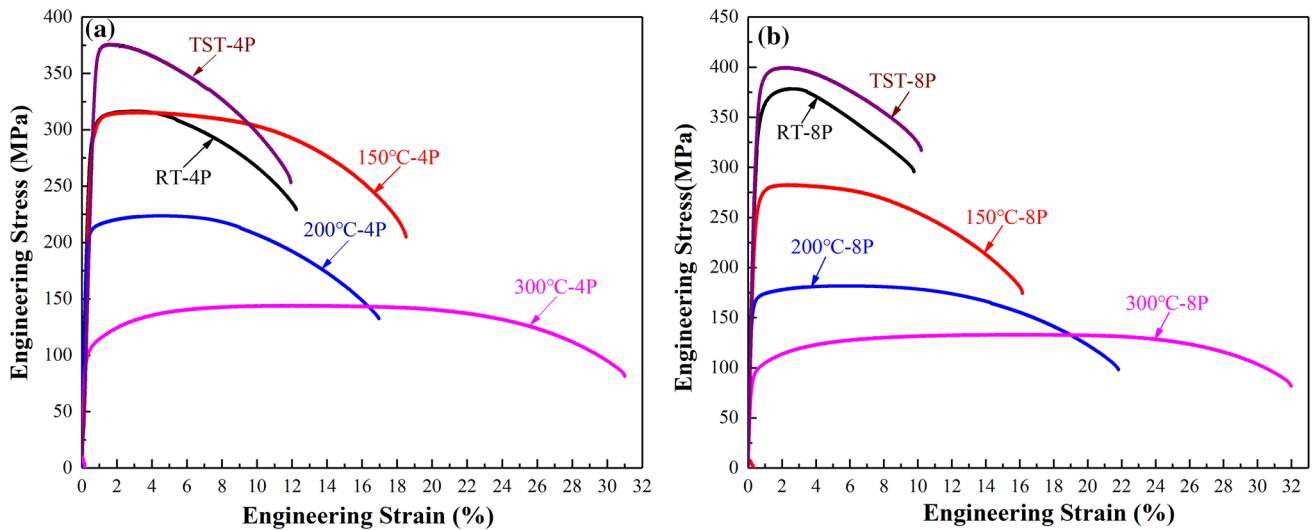


Fig. 2 Engineering stress–strain curves of the 6063 Al alloy processed by ECAP after four passes **a**, and eight passes **b** in different ECAP processing conditions

Table 1 Mechanical and electrical properties of the 6063 Al alloy processed by ECAP under different conditions

State	Mechanical properties			Electrical conductivity ρ (% IACS)
	YS (MPa)	UTS (MPa)	Elongation (%)	
RT-4P	299	317	13.9	48.3
RT-8P	346	378	9.8	47.7
TST-4P	366	376	12	49.5
TST-8P	373	400	10.7	48.2

The hardness and conductivity of samples subjected to four-pass ECAP processing at RT and TST conditions and post-ECAP aging treatment are shown in Fig. 3. For RT four-pass ECAP sample, the hardness remained reasonably constant in the aging time to 24 h at 120 °C, but it decreased dramatically at 150 °C with increasing aging time and drop to 91 Hv after aging for 24 h. These annealing curves reveal that the high hardness of four-pass sample processed at TST condition cannot be reached for the sample processed by a

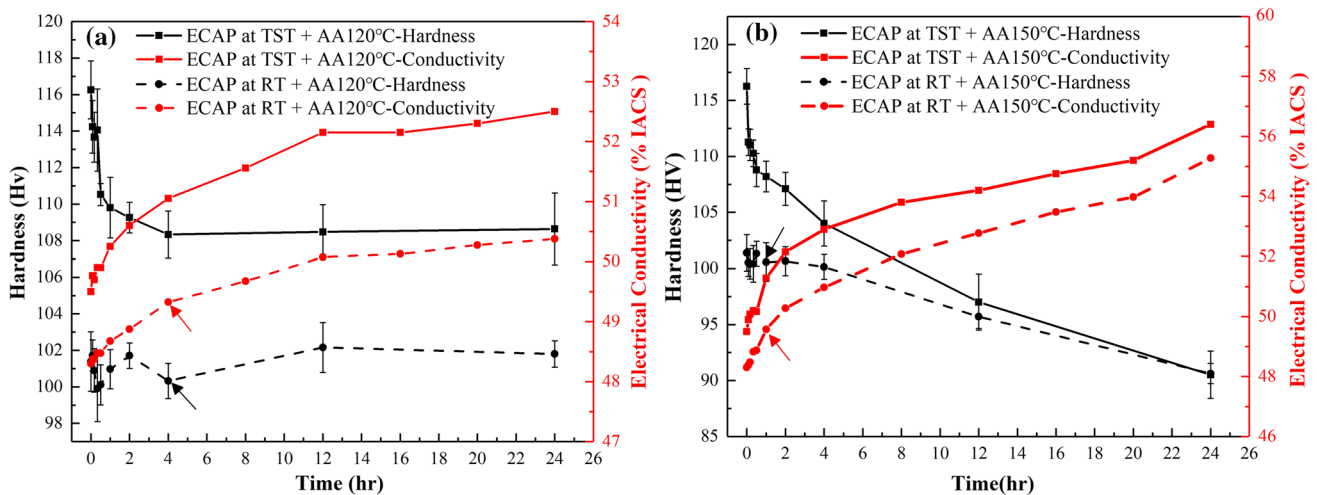


Fig. 3 Evolution of the micro-hardness and electrical conductivity of the 6063 Al alloy processed by four-pass ECAP processing at RT and TST conditions as a function of the post-ECAP annealing time for artificial aging treatment at 120 °C **a** and at 150 °C **b**

combination of ECAP processing at RT condition and subsequently aging treatment (at 120 °C and 150 °C). The post deformation aging treatment leads to a general increase of the electrical conductivity in RT samples and TST samples, as observed for Al–Mg–Si alloys [8]. Although the electrical conductivity of RT four-pass ECAP sample after post-ECAP aging (as indicated by red arrows in Fig. 3) increase into ~49.5% IACS, similar to that of TST four-pass ECAP sample, the corresponding hardness (as indicated by black arrows in Fig. 3) is 16 Hv lower than that in TST four-pass ECAP sample. In addition, processing at TST condition produced a better combination of strength and conductivity during the whole duration of the aging treatment compared to RT counterparts.

3.2 ECAP-Induced Microstructural Evolution

Figure 4 shows the characteristic microstructures of the 6063 Al alloy before ECAP processing. The as-received alloy has a microstructure consisting with coarse equiaxed grains with an average grain size about 177 μm , which have been enclosed by platelets-like Fe-rich intermetallic by EDS analysis (Fig. 4c). As shown in Fig. 4b, some bar-like phases existed in the interior of grains with the means width of 0.13 μm and the length ranged from 0.3 to 1.8 μm . These phases were identified as $\beta\text{-Mg}_2\text{Si}$ by EDS analysis (Fig. 4d). By comparison, notable dissolution of these Mg_2Si phases into Al matrix occurred after a solution treat, as shown in Fig. 4e. However, the mean grain size almost remained the constant.

Typical optical microstructures evolved in the 6063 Al alloy processed at different temperatures are shown in Fig. 5. As shown in Figs. 5a–c, after one pass, the initial equiaxed coarse grains were highly elongated with a mean grain size of 530 μm parallel to the direction of elongation and 60 μm perpendicular to the direction, leading to an aspect ratio about 8.8 which do not depend much on the ECAP processing temperature. The intense concentration of strains in deformation bands and shear bands developed in the one-pass samples. These bands are associated with the considerable strain gradients introduced by deformation-induced heterogeneous strain [21]. After further passes, the coarse grains can be subdivided by intersection of these bands (Fig. 5d–l). At high deformation strains, processing at RT and 150 °C led to some thinner shear bands merging into large bands (indicted by dark dotted circles in Fig. 5). In comparison, after four and eight passes at 300 °C (Fig. 5i and l), the tendency for the shear bands became less common and fine-grained bands appear along shear direction due to high dynamic recovery rate and preferent relaxation of strains in shear bands.

Figure 6 shows that the TEM micrographs of the two-pass and eight-pass samples processed by ECAP at RT, 150 °C and 300 °C. This figure indicates that two- and eight-pass processing at 300 °C produced coarser equiaxed grains compared to at RT and 150 °C with a mixture of elongated and equiaxed ultrafine grains. Moreover, the sample processed at 150 °C had a smaller mean subgrain width (0.325 μm) than that of processing at RT (0.349 μm) if the number of ECAP passes was two. However, in the case of eight-pass condition, the sample processed at RT had a smaller mean

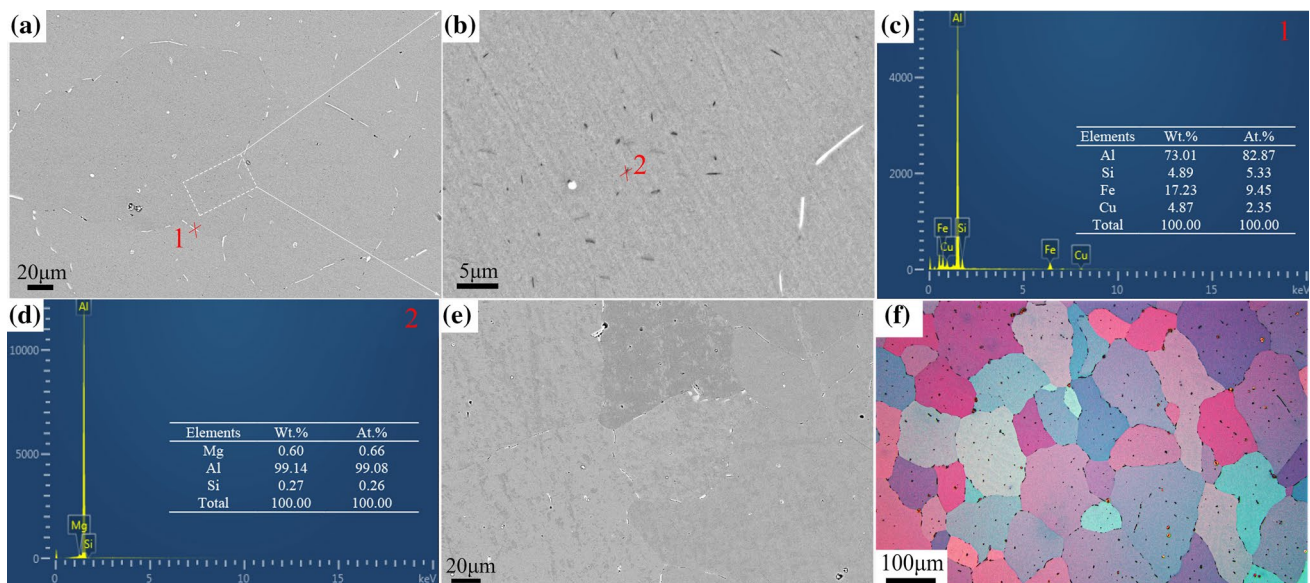


Fig. 4 Microstructures of the 6063 Al alloy before ECAP process: **a** SEM image of as-received material, **b** SEM image of the enlarged zone marked in **a**, **c** and **d** the corresponding EDS analysis marked in **a** and **b**, **e** SEM and **f** polarized light images of solution-treated material

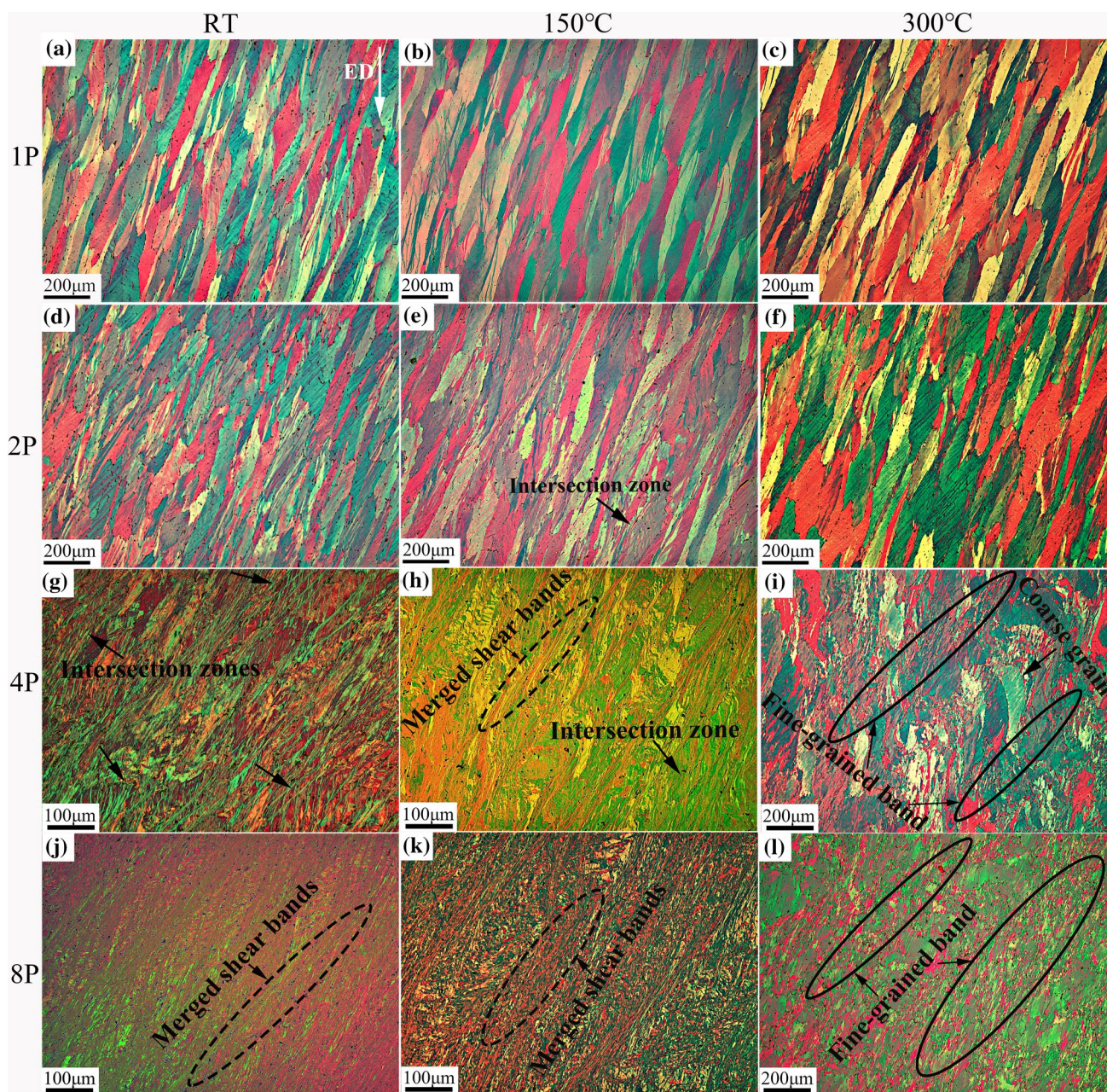


Fig. 5 Polarized light microstructures of the 6063 Al alloy processed by ECAP after one pass at RT **a**, 150 °C **b** and 300 °C **c**, two passes at RT **d**, 150 °C **e** and 300 °C **f**, four passes at RT **g**, 150 °C **h** and 300

°C **i**, and eight passes at RT **j**, 150 °C **k** and 300 °C **l**. The white arrow indicates the extrusion direction (ED)

(sub)grain width (0.19 μm) than that of processing at 150 °C (0.407 μm). Analysis of the SAED patterns in Fig. 6 shows that the scattered spots in the SAED pattern for two-pass samples (Fig. 6a and b) evolved into ring pattern consisting of discrete spots for eight-pass samples processed at both RT and 150 °C (Fig. 6d, e), indicating that successive processing at the RT and 150 °C can lead to most of (sub)grains boundaries having medium to high angles of misorientation [14, 22].

Figure 7a and b show the TEM micrographs of the samples after four-pass and eight-pass ECAP processing at TST condition, respectively. As a comparison, the TEM micrographs of the samples after four-pass ECAP processing at RT, 150 °C are also shown in Fig. 7c and d, respectively. The histograms of substructure size distributions of the 6063 Al alloy processed by four and eight passes at RT, 150 °C and TST conditions are presented in Fig. 8. The substructure size is the width in the transverse of elongated (sub)grains. The

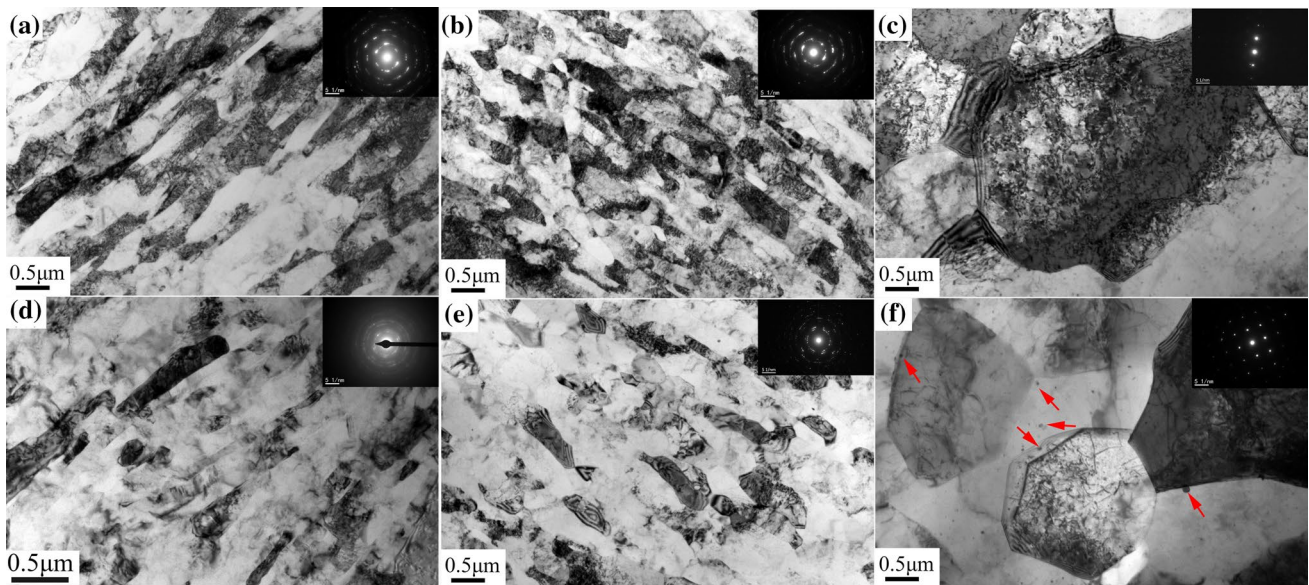


Fig. 6 Representative TEM BF images of samples processed by ECAP after two passes at RT **a**, 150 °C **b** and 300 °C **c**; eight passes at RT **d**, 150 °C **e** and 300 °C **f**. The red arrows point at precipitates in **f**

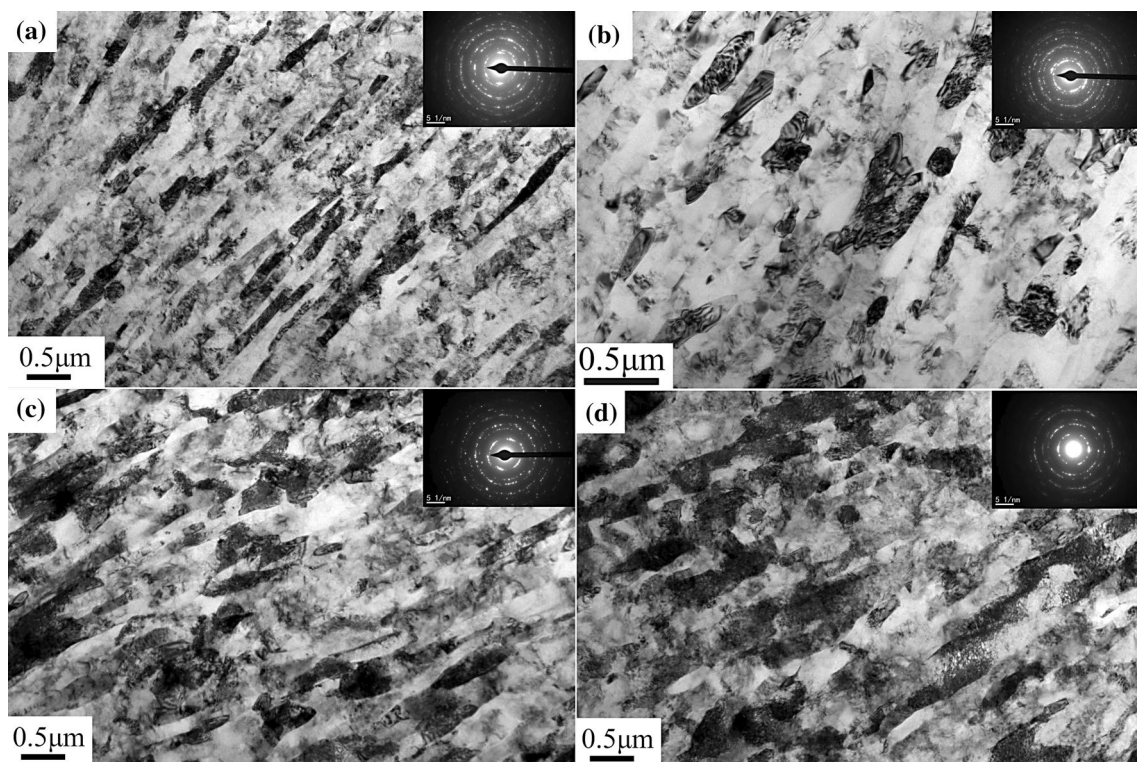


Fig. 7 Representative TEM BF images of samples processed after four passes **a** and eight passes **b** at TST, and after four passes at RT **c** and at 150 °C **d**

d_w in Fig. 8 is the effective mean width of (sub)grains and was determined from TEM images using $d_w = \left(\frac{\sum_i f_i d_i^2}{\sum_j f_j d_j^3} \right)^{-1}$ [8], where f_i is the proportion of

(sub)grains with a mean width d_i in Fig. 8, and at least 200 objects were measured to make statistical comparisons. The mean (sub)grain width of the samples processed by four and eight passes at TST condition are 0.235 and 0.197 μm ,

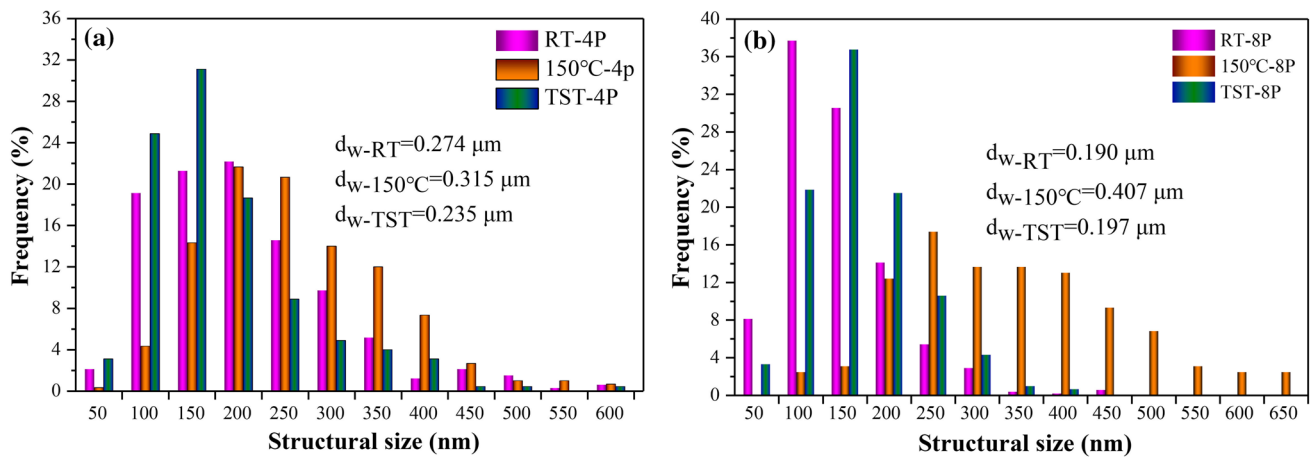


Fig. 8 Histograms of structural size distribution for samples processed at different conditions: (a) four passes; (b) eight passes

respectively. The SAED patterns in Fig. 7 also indicate that (sub)grain boundaries mostly exhibit large misorientations. The equivalent grain width of four-pass samples processed by three conditions is in the order of $150^\circ\text{C} > \text{RT} > \text{TST}$, indicating that processing at TST condition produced the better grain refinement.

Figure 9 shows that the bright field (BF) TEM images with the corresponding selected area diffraction patterns, and Fig. 10 shows that the HRTEM images and HAADF-STEM images with the corresponding Fast Fourier Transformation (FFT) patterns for the samples processed at different processing temperatures. Processing at RT brought out only few precipitates locally as shown in Fig. 9a and b. In contrast, a large density of sphere-like GP zones with a diameter of only few nanometers were exhibited in the samples processed by one and two passes at 150°C . These GP zones displayed some typical strain-field contrast in.

Figure 9c and d. The high resolution of GP zone is presented in Fig. 10a. The atomic intensity line profile inserted in the Fig. 10a suggests that the diameter of the GP zone is about 4.6 nm. In line with the precipitation sequence of the Al–Mg–Si alloys, GP zones form in the very early-stage of precipitation during aging. As presented in Fig. 9c and d, the density of nanoscaled precipitates pronouncedly increase with the number of passes from one to two at 150°C .

After one-pass processing at 200°C , a large quantity of needle-like precipitates with 10–38 nm in length can be noticed, as illustrated in Fig. 9e. HRTEM observations further revealed that the majority of these needle-shaped precipitates were the monoclinic β'' -phase (Fig. 10b and c) [23–25]. They appeared as black lines which are different from its typical morphology in coarse-grained materials during annealing with no strain-field contrast at the center of the needle due to the strong strain contour in the vicinity of the needle while full coherency with the Al matrix in its interiors [26, 27]. Moreover, some precipitates present the unit cell structure and orientation relationship

for the hexagonal β' -precipitate (Fig. 10d): $a = b = 0.715 \text{ nm}$, $\gamma = 120^\circ$, $\langle 2-1-10 \rangle_{\beta'}/\langle 100 \rangle_{\text{Al}}$ [28].

In Fig. 9f, some relatively coarse bar-like particles, with diameter and length up to 40 nm and 120 nm, respectively, are visible in the sample processed by one-pass ECAP at 300°C . Judging from elements mapping of these precipitates in Fig. 10e, they should be Mg–Si phases. The EDS spectra of some typical precipitates (as shown in Fig. 9) indicate that these precipitates occurred with the Mg/Si ratio close to 2, which is consistent with β' (Mg_9Si_5) and β (Mg_2Si). These precipitates may be the post- β'' phases in the precipitation sequence. It also confirms that these precipitates have indeed formed from the matrix in the one-pass sample processed at 300°C , independence of the early-stage Mg–Si phase. At same time, some coarse precipitates with a cross-section about 40 nm in a diameter are identified as β' precipitates in this state as shown in Fig. 10g due to typical β' spots circled in yellow in the inserted FFT pattern [28].

Figure 11 displays precipitation characteristics of four-pass samples processed at 150°C and TST conditions and eight-pass sample processed at TST condition. A large density of sphere shaped precipitates were still present in these samples. These nanoscaled precipitates exhibit a typical size about only few nanometers. These observation are quiet consistent with the data reported for GP zones of the samples processed after one and two passes at 150°C , and it is possible to determine these precipitates to be GP zones, as indicated by the HRTEM image inserted in Fig. 11b [26].

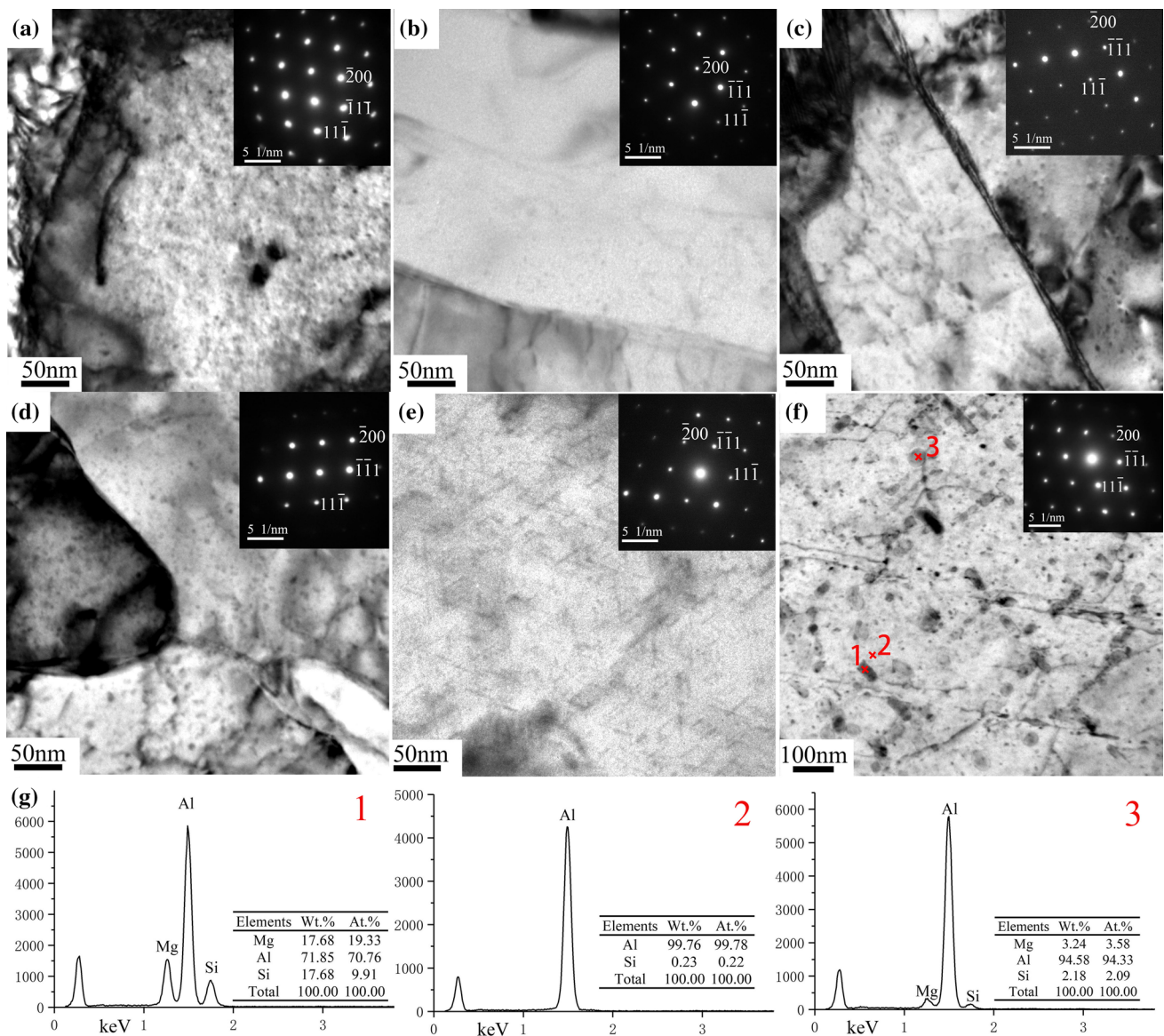


Fig. 9 TEM BF images of sample processed after (a) one pass and (b) two passes at RT; (c) one pass and (d) two passes at 150 °C; (e) one pass at 200 °C and (f) at 300 °C; (g) EDS spectra of points in (f). TEM BF image were obtained in the $\langle 011 \rangle$ Al axis

4 Discussion

4.1 Influence of the Processing Temperature on UFG Microstructures

As compared with processing at other temperatures, processing at 300 °C produced coarse grains in several micrometers as observed in Fig. 6. It is expected that the increase in grain size is related with a high rate of dynamic recovery as processing at high temperature [6]. Such an increase in the grain size of SPD-processed sample with the increasing of processing temperature has been widely observed in many alloys [10, 29]. However, the (sub)grain size of

two-pass sample processed at 150 °C is smaller as compared to the counterpart processed at RT. At the same time, after four passes, processing at TST condition produced the smaller grain size as compared to processing at homologous temperature (RT and 150 °C). It is expected that the grain refinement should be also associated with precipitates and decomposition of the supersaturated solid solution during processing. Unlike the processing at RT condition, a large number of nanoprecipitates formed in the samples processed by two passes at 150 °C and four-pass at TST, which can play an important role in retarding migration of grain boundary. On the other hand, after eight-pass ECAP processing at 300 °C, the large precipitates formed near the grain boundary,

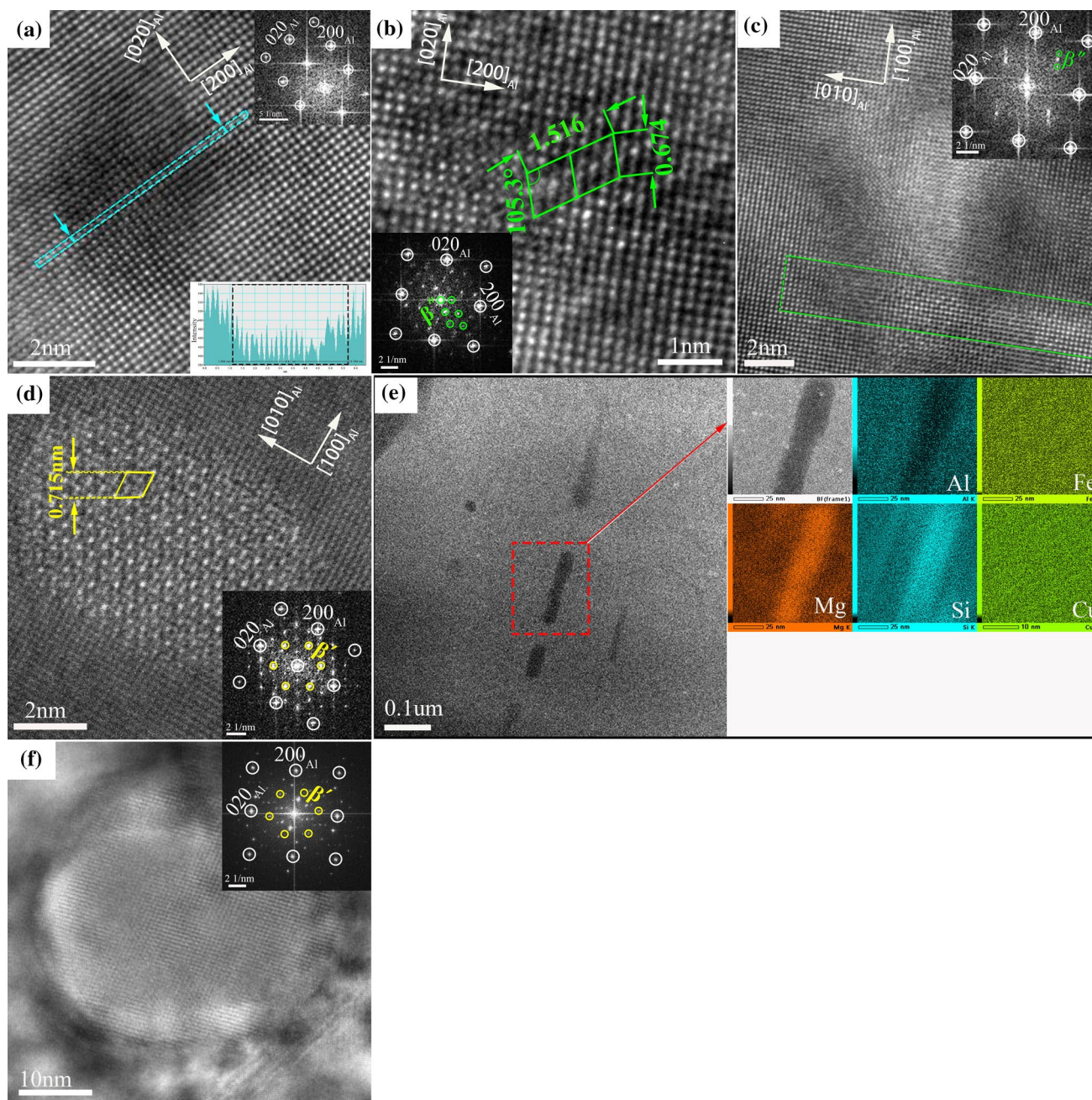


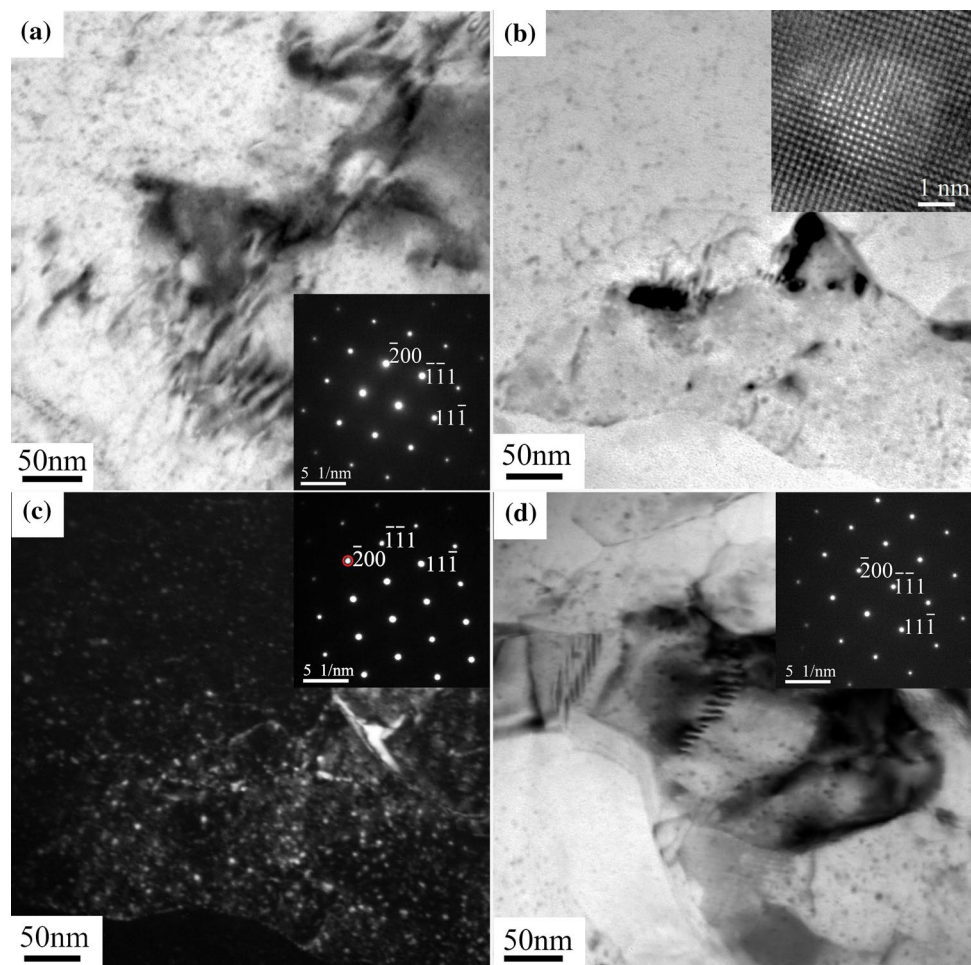
Fig. 10 The precipitates in the Al–Mg–Si alloy processed by ECAP: (a) HRTEM image of the sample processed after two passes at 150 °C; (b), c HRTEM images and (d) HAADF image of the sample processed after one pass at 200 °C; (e) HAADF-STEM images and cor-

responding STEM-EDS maps, and (f) HRTEM image of the sample processed after one pass at 300 °C. TEM images were obtained in the $\langle 001 \rangle$ Al axis

suggesting that solute atoms may segregate in the grain boundaries during SPD processing, which has been already observed in UFG Al alloys [10, 14]. Some segregates transformation to grain-boundary precipitates after aging has been confirmed Al–Zr alloy [14]. Processing at RT could produce limited degree of decomposition of the matrix and few solute atoms segregated on the grain boundaries, leading

to a coarser grain size in the two-pass sample processed at RT than that at 150 °C. This suggestion is consistent with the situation that the better grain refinement is obtained in the alloy processed in the TST condition with nanoprecipitates formed by a low degree of decomposition and simultaneously a level of solute atoms probably segregated at grain boundaries. Moreover, it has been observed that a level of

Fig. 11 TEM BF images of samples processed after four passes at 150 °C **a**, TST **b**, and after eight passes at TST **d**; according TEM DF image of the sample processed after four passes at TST **c**. TEM BF images were obtained in the $\langle 011 \rangle_{Al}$ axis. A typical HRTEM image of precipitates in the four-pass sample processed at TST from $\langle 001 \rangle_{Al}$ axis is also shown in the inset of **b**



decomposition about 20% solute atoms formed into small precipitates together with the maximized segregation of solute atoms at grain boundaries produce the strongest grain refinement [30], which might be argued to be the case in the present study. Thus, it is concluded here that grain size is not only control by the dynamic recovery of crystallographic defects induced by severe deformation but also by the decomposition of the alloy, precipitation and segregation of solute atoms.

In comparison with RT condition, the pronounced precipitates in the samples processed at temperatures from 150 to 300 °C. As revealed by TEM results in Figs. 9 and 10, an increase of processing temperature in the range of RT–300 °C does not change the expected precipitation sequence in low-alloy Al–Mg–Si alloys. However, ECAP processing temperatures affect metastable precipitates formation and thus the properties of the 6063 alloy. Figure 12 shows the electrical conductivities and ultimate tensile strengths of one-pass samples. In the case of one-pass ECAP samples with a similar grain size, the electrical conductivity can be used to estimate the changes of solid atoms content in the matrix. With an increase in temperature from RT to 300 °C, the increased diffusion kinetics enhance

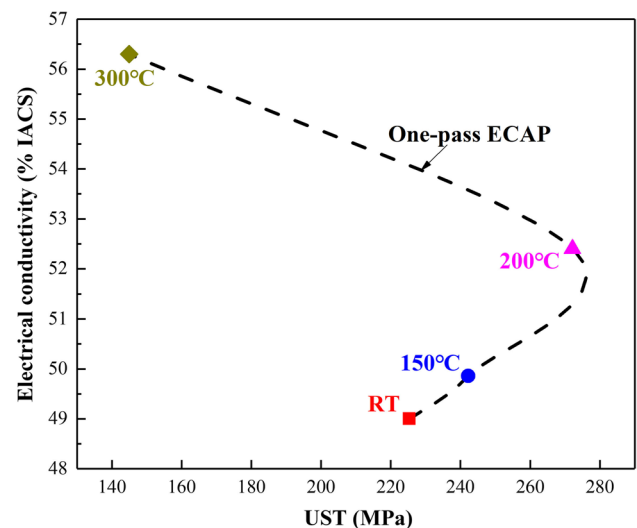


Fig. 12 Plot of the electrical conductivity versus ultimate tensile strength (UTS) of one-pass samples processed at different temperatures

the decomposition of the alloy. This suggestion is consistent with the increased electrical conductivity with increasing of processing temperature, since the Mg and Si in the matrix can significantly deteriorate the conductivity [31, 32]. Moreover, with increasing in the number of passes to two, processing at 150 °C produces an obvious increase in the volume fraction of the nanosized precipitates, which is probably assisted by the ECAP-induced high-density dislocations through dislocation-core diffusion mechanism [33]. Under TST condition, there was a litter change in the volume fraction of nanoscale precipitates with increasing number of passes from four to eight, suggesting that these nanoscale precipitates originating from two-pass processing at 150 °C may remain in the following passes at TST condition.

4.2 Contributing Factors to the High Strength and Reasonable Electrical Conductivity of Samples Subjected to Two-Step Pressing

The 6063 Al alloy processed at RT condition have demonstrated the enhancement in the strength with increasing the number of passes. The yield strength different of 140 MPa between samples processed at RT from one to eight passes appear to be correlated with the enhanced strengthening contribution from the grain refinement from 56 μm to 0.19 μm. However, the strength of the sample after four-pass ECAP processing at TST condition is 366 MPa, even slightly higher than that in sample after eight-pass processing at RT (346 MPa) with a smaller grain size. The most significant microstructural features of the sample in TST condition are the nano-scale precipitates and high-density dislocations. As a result, it is deduced that these features play a key role in the increase of strength in the TST sample. Based on the above the investigation about microstructures, it indicates that the following strength mechanisms should be considered for the investigated alloy: grain boundary strengthening, precipitation strengthening, solid solution strengthening and dislocation strengthening. Assuming contributions from different strengthening constituents act independently, the total strength is given by [14, 34].

$$\sigma_y = \sigma_0 + \sigma_{GB} + \sigma_{ss} + \sigma_{dis} + \sigma_p \quad (1)$$

where σ_y is the yield stress, σ_0 is the lattice friction stress, σ_{ss} , σ_{dis} , σ_{GB} , and σ_p are contributions from the solutes in solid solution, dislocations, grain boundaries and precipitates, respectively. For the pure Al, the lattice friction stress has a value of 10 MPa [19].

The influence of solid solution hardening might be written as [35, 36]

$$\sigma_{ss} = \sum k_i c_i^{2/3} \quad (2)$$

where k_i is a scaling factor for the solute i , and c_i is the concentration of the solute in weight percent wt%. The

scaling factors k_i of the Mg and Si are 29 MPa (wt.%)^{-2/3} and 66.3 MPa (wt.%)^{-2/3} [35], respectively. Assuming all the solute atoms (0.52% Mg, 0.49% Si) are in the solid solution and contributions of these atoms are simple additive, the increase in yield strength due to solid-solution strengthening in the investigated alloy is about 60 MPa. However, precipitation and SPD induced segregation on the grain boundaries might lead to a decrease of the solutes in the matrix of the TST samples. Hence, 60 MPa is an upper bound for the samples at TST condition. On contrast, due to some limited precipitates in RT samples, the contribution of solid-solution might be very close to 60 MPa. As shown in Fig. 13, the estimated solid solution hardening in four-pass and eight-pass samples at RT condition shows a variation of 51–61 MPa.

The contribution of dislocations to the yield stress increase might be estimated through the following relationship [37]:

$$\sigma_{dis} = aMGb\rho^{1/2} \quad (3)$$

$$\rho = 2\langle \varepsilon^2 \rangle^{1/2} (D \times b) \quad (4)$$

where a is a constant (0.3) for the FCC phase, M Taylor factor (3.06), G shear modulus (26.9 GPa), b Burgers vector (0.29 nm) and ρ is the dislocation density determined using Eq. (4). The coherent scattering domain D and the elastic microdistortion level $\langle \varepsilon^2 \rangle^{1/2}$ can be calculated from XRD peak broadening (B) by employing the Williamson-hall methodology [20, 38, 39]. Dislocation strengthening leads to strength increment of about 72 MPa and 37 MPa for the four-pass samples processed at TST and RT conditions, respectively.

The contribution of grain boundary strengthening in UFG materials can be analyzed by Hall–Petch relationship [19, 34].

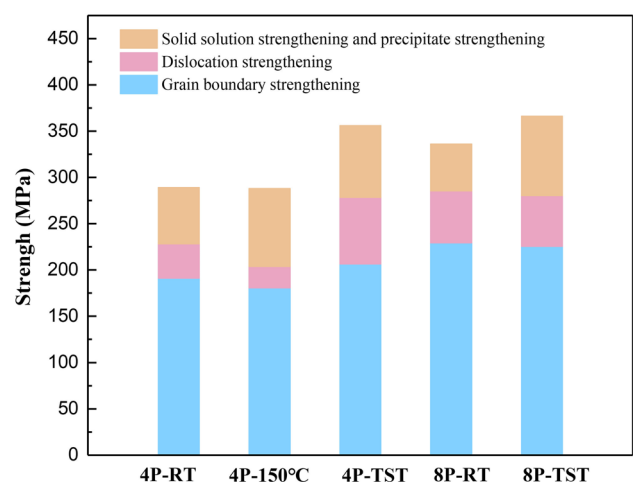


Fig. 13 The estimated stress form different strengthening mechanisms

$$\sigma_{GB} = k_y d^{-1/2} \tag{5}$$

where k_y is the strengthening coefficient constant, which is considered as 0.1 MPa·m^{1/2} in Al alloys [40]. These investigated samples are characterized with the elongated structure, and high strains lead to a decrease in its width (d_w). It has been illustrated that the strength caused by grain boundary strengthening increases with decreasing the width of the elongated structure, in accord with Hall–Petch relationship, in the pure Al processed by cold drawing [41], commercial purity copper proposed by ECAP [42], and Al–Cu alloy processed by surface mechanical grinding treatment at liquid nitrogen temperature [10]. In the analysis of grain boundary strengthening in present study, the width of elongated structure can be reasonably taken as a strength determining parameter. The strength increment from the strengthening is calculated to be 184, 229 and 206 MPa in samples processed by four and eight passes at RT condition and four passes at TST condition, respectively.

The contribution from precipitates can be calculated by Refs. [43, 44]:

$$\sigma_{orowan} = \frac{0.13Gb}{L_p} \ln(r/b) \tag{6}$$

In this equation, G and b are the shear modulus ($G=25.8$ GPa) and the Burgers vector ($b=0.286$ nm) of the matrix, respectively, r is the mean radius of a circular cross-section for a spherical precipitates, and L_p is the inter-precipitate distance and can be expressed by the following equation [43].

$$L_p = r \left(\sqrt{3\pi/(4f)} - 2\sqrt{2/3} \right) \tag{7}$$

where f is the volume fraction of precipitates, which can be roughly estimated by the Eq. 8 [18].

$$f = \left(\frac{N}{S} \right)^{\frac{2}{3}} \times \frac{4}{3} \times \pi \times r^3 \tag{8}$$

where N is the number of the precipitates, S the total area of the measured region, and r the mean radius of precipitates. Based on the TEM observations, the volume fraction of nano-precipitates in the four-pass samples processed at 150 °C and TST conditions and eight-pass sample processed

at TST conditions were estimated as 1.5%, 0.3% and 0.5%, respectively, with an average radius of 1.39 nm, 1.72 nm and 1.15 nm. Thus, the contribution of precipitates to the strengthening through Orowan mechanism are estimated 101 MPa, 39 MPa and 60 MPa for these three samples, respectively. The contribution of precipitates strengthening in the sample processed at RT can be neglected since few precipitates were detected in the grains.

A summary of contributions from different strengthening mechanism is shown in Table 2. For the samples processed by four and eight passes at RT, the calculated total strengths are in very good agreement with the experimental data (σ_{exp}), respectively, which suggests that the quantitative calculations from different strengthening mechanism are appropriate on the above discussions. On contrast, as for these two samples processed at TST condition, the calculated values are smaller than the experimentally-measured stresses. One explanation for the slight high difference is partly decomposition of solid solution during ECAP processing at TST condition, probably indicating that some solutes may still retain in the Al matrix and can lead to an increase in the strength through solute-solution strengthening.

On the other hand, in order to quantify the significance of nano-precipitates strengthening as compared with solid-solution strengthening, it should further estimate the value of $\sigma_{ss} + \sigma_p$ in these samples. In the case of sample processed at RT condition, the $\sigma_p \approx 0$, and $\sigma_{ss} = \sigma_{exp} - (\sigma_{GB} + \sigma_0) - \sigma_{dis}$. For the sample processed at 150 °C and TST conditions, $\sigma_{ss} + \sigma_p = \sigma_{exp} - (\sigma_{GB} + \sigma_0) - \sigma_{dis}$. Figure 13 shows the contributions from the different strength mechanisms for the samples processed at different conditions. As given in Table 2 and Fig. 13, the major strengthening mechanism is grain boundary strengthening through Hall–Petch effect, which accounts for at least 60% of a total contribution in these investigated samples. Moreover, the calculated levels $\sigma_{ss} + \sigma_p$ for the samples at 150 °C and TST conditions are higher than the values from solid-solution strengthening in the samples at RT (as shown in Fig. 13), suggesting that nano-precipitates play a more significant role in strengthening. It has proved that the nanoprecipitates can be obstacles and sourced of dislocations, and be responsible for the high tensile strength [17]. In present study, the nanosized precipitates could promote a high-density dislocation, fast up to the saturation level. This explains the

Table 2 The calculated stress by different strengthening mechanisms in comparison with experimental stress

State	Calculated stress (MPa)						Experimental stress σ_{exp} (MPa)	Differnt stress $\Delta\sigma$ (MPa)
	σ_0	σ_{GB}	σ_{Dis}	σ_{ss}	σ_p	$\sigma_{0.2}$		
150 °C-4p	10	181	23	–	101	314	298	17 MPa (5.6%)
TST-4p	10	206	72	–	39	327	366	39 MPa (11%)
TST-8p	10	225	55	–	60	350	376	26 MPa (6.8%)
RT-4p	10	191	37	60	0	298	299	1 MPa (0.3%)
RT-8p	10	229	56	60	0	355	346	9 MPa (2.7%)

reason why dislocation strengthening in four-pass samples processed at TST condition produce an extra increase in strength as compared with four-pass and eight-pass at RT condition. During SPD processes the density of dislocation might reach a saturation value while thereafter further strains could lead to a reduction of its density, which have been also previously observed HPT-processed pure Al [45] and ECAP-processed Al–Mg–Si alloys [16].

Similar to the analysis of strengthening mechanism, it is possible to investigate contribution of each microstructural features to the electrical conductivity. Since it has been showed that the theoretical predictions of electrical conductivity by using the Matthiessen's rule is a relatively good agreement with experimental values [8, 14], contributions from the crystalline defects in the investigated samples in present study can be quantified by it. According to the Matthiessen's rule, the total resistivity of the alloy can be expressed as:

$$\rho_{total} = \rho_{Al} + \rho_{Vac} + \rho_{Dis} + \rho_{GB} + \rho_{SS} + \rho_{Pt} \tag{9}$$

Here, ρ_{Al} is the resistivity of pure Al at room temperature which is equal to 26.55 nΩm. The $\rho_{Vac}, \rho_{Dis}, \rho_{GB}, \rho_{SS}$ and ρ_{Pt} are the increases in resistivity due to the vacancies, dislocations, grain boundaries, solute atoms in the matrix and precipitates, respectively.

The contribution of vacancy to the resistivity could be estimated as follows [46]:

$$\rho_{Vac} = C_v \Delta\rho^{Vac} \tag{10}$$

where C_v (at.%) is the concentration of vacancies, and $\Delta\rho^{Vac} = 26 \text{ n}\Omega\text{m/at.}\%$ [47]. It has been observed that the SPD processing may lead to a significant increase in the vacancy concentration up to the $10^{-3}\%$ [48]. However, even for such a high vacancy concentration, the contribution of vacancies is as small as 0.026 nΩm. Therefore, the influence of the vacancy on the resistivity is not important and has been ignored in the samples of the present study.

The contribution of dislocations to the resistivity could be calculated by the following equation [46]:

$$\rho_{Dis} = L_{Dis} \Delta\rho^{Dis} \tag{11}$$

Here, the $L_{Dis} \text{ (m}^{-2}\text{)}$ is the dislocation density, and $\Delta\rho^{Dis} = 2.7 \times 10^{-25} \text{ }\Omega\text{m}^3$ [8, 31]. The role of dislocations on the resistivity can be estimated based on the XRD results.

Even though the high-density dislocations were generated in the samples during ECAP processing, the increase in resistivity from dislocations does not exceed 0.027 nΩm. Thus, the contribution may still be neglected as compared with grain boundaries, solute atoms and precipitates.

The contribution of grain boundaries on the resistivity can be also calculated as [49]

$$\rho_{GB} = S_{GB} \Delta\rho^{GB} \tag{12}$$

where the $S_{GB} \text{ (m}^{-1}\text{)} \approx 2/d_{av}$ [34] is the fraction of the grain boundary per unit volume in a material with an equivalent mean grain size d_{av} , and $\Delta\rho^{GB} = 2 \times 10^{-16} \text{ }\Omega\text{m}^2$ [49]. In the present study, the equivalent mean grain width (d_w) is used to obtain an upper bound of the contribution of grain boundaries.

Additionally, the mutual resistivity of solute atoms (Mg and Si) and precipitates can be calculated by a difference between total resistivity and the contributions of pure Al and grain boundaries to the resistivity of the 6063 Al alloy, $\rho_{SS} + \rho_{Pt} \approx \rho_{Total} - (\rho_{Al} + \rho_{GB})$. Following to the approach, the obtained each contribution is summarized in Table 3. In this context it is the noteworthy that the value of $\rho_{SS} + \rho_{Pt}$ in Table 3 might be considered as a lower bound, since the contribution of grain size is overestimated. Even then, it is clear that the conductivity is extremely sensitive to the values of $\rho_{SS} + \rho_{Pt}$ in these investigated samples, which contributes to 14%–21% of the total electrical resistivity. Based on the microstructural features, samples in 150 °C and TST conditions achieved higher electric conductivity could be attributed to nano-scale precipitates compared to RT samples. This suggestion is in line with the general trendies of electric conductivity of samples processed at 150 °C and RT in present study. The grain refinement may be responsible for a reduction of the electrical conductivity with the number of passes in RT samples. On contrast, even though the grain size significantly decreases from one to two passes as processing at 150 °C (in Fig. 5), an increasing density of nano-scale precipitates might lead to an increase of the electrical conductivity (49.86%IACS of one-pass sample, 50.3%IACS of two-pass sample). Thus, solute atoms formed into the precipitates should be mainly responsible for the increase in the electrical conductivity. The second important microstructural

Table 3 Influence of different microstructural features on the electrical resistivity

State	$\rho_{Total}(\text{n}\Omega\text{m})$	$\rho_{Al}(\text{n}\Omega\text{m})$	$\rho_{Vac}(\text{n}\Omega\text{m})$	$\rho_{Dis}(\text{n}\Omega\text{m})$	$\rho_{GB}(\text{n}\Omega\text{m})$	$\rho_{SS} + \rho_{Pt}(\text{n}\Omega\text{m})$
150 °C-4p	32.7	26.55	0.026	0.009	1.65	4.5
TST-4p	34.83	26.55	0.026	0.027	2.19	6.087
TST-8p	35.77	26.55	0.026	0.021	2.64	6.55
RT-4p	35.7	26.55	0.026	0.014	1.77	7.38
RT-8p	36.15	26.55	0.026	0.021	2.74	6.86

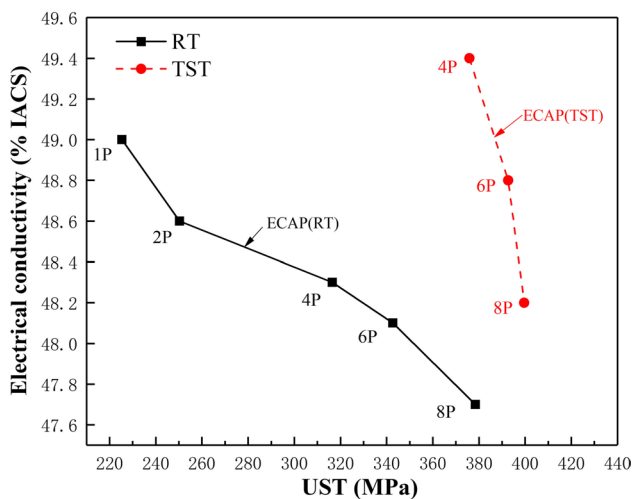


Fig. 14 Ultimate tensile strength (UST) and electrical conductivity of the 6063 Al alloy processed by ECAP under RT and TST conditions

feature affecting the conductivity is grain boundaries with 5%–7% contribution to the electrical resistivity.

Besides, the types of precipitates may have effects on the increase of electrical conductivity [19, 50]. ECAP processing at TST condition may lead to presence of coherent nanoprecipitates. On comparison, ECAP processing at 300 °C led to formation of pronounced post- β' phases and thus a high electrical conductivity (up to 57.2%IACS, but a very low strength about 145 MPa). Such an increase of electrical conductivity has been observed Al 6101 alloy with the formation of dominant β' and β phases after HPT processing at RT and post-HPT annealing [8] and Al 6201 alloy with precipitation of β' after warm HPT processing [19]. For further improvement of electrical conductivity concurrent with a high strength of the alloy, the first temperature regime of the two-step processing may be conducted at an elevated temperature (above 150 °C) followed at a relatively low temperature (such as RT) to obtain an UFG structure with a high density of nanoprecipitates in semi-coherent or even non-coherent states.

The combination of strength and electrical conductivity of the samples processed at RT and TST conditions is given in Fig. 14 Compared to the RT condition, a better combination of mechanical property and conductivity of the 6063 Al alloy could be achieved by the TST method. The nanoscaled precipitates in TST condition can be effective at suppressing the grain boundary migration, pinning dislocations, and purifying the alloy matrix. This highlights the important of nanoprecipitates for the high strength and conductivity, which can break the mutually exclusive relationship between the strength and conductivity, as suggested recently in Al–Zr alloy after ultra-SPD [14]. It is concluded here that the processing condition able to produce the better combination properties in low-alloyed Al–Mg–Si alloys is the one at which a larger number of

nanoscale phase precipitate from decomposition of supersaturated solid solution, in combination with the ultrafine grains. Hence, the TST approach seems to be an effective approach to simultaneously enhance strength and electrical conductivity for the low-alloyed Al–Mg–Si alloy.

5 Conclusions

The effects of ECAP processing temperatures on microstructures, mechanical and electrical properties of the Al–Mg–Si alloy were investigated, and a two-step temperature schedule (TST) was present to produce the low-alloyed Al–Mg–Si alloys with the optimum combination properties. The following findings and conclusions are reached.

1. Grain size and precipitation were highly dependence on the ECAP processing temperatures and applied strains. Of different processing conditions, processing at TST condition led to the best grain refinement.
2. Unlike the RT condition, processing at TST condition is characterized by lower strains required for the high yield strength and reasonable electrical conductivity (366 MPa and 49.5%IACS of four-pass TST sample, 299 MPa and 48.3%IACS of four-pass RT sample).
3. Theoretical analysis shows that maximal contribution to strength arise from the grain boundary strengthening. A large number of nano-precipitates and a high-density dislocation play the significant roles on the strength increment in the ECAP-processed 6063 Al alloy. The electrical conductivity is mainly related to the solute concentration in the matrix. The nanoscaled precipitates can contribute additional strengthening and purify the alloy matrix simultaneously, which are responsible for the excellence combination properties in TST samples.
4. This work reveals that the ultrafine grains with nanosized precipitates, which can be induced by the ECAP processing under TST condition, are very effective in achieving the better combination of strength and electrical conductivity in the low-alloyed Al–Mg–Si alloy.

Acknowledgements This work was supported by the National Natural Science Foundation of China (51874091).

Declarations

Conflict of interest The authors declare no conflict of interest.

References

1. R.Z. Valiev, R.K. Islamgaliev, I.V. Alexandrov, *Prog. Mater. Sci.* **45**, 103 (2000)
2. M. Cabibbo, *Mater. Sci. Eng. A* **785**, 139348 (2020)

3. O. Sitdikov, R. Garipova, E. Avtokratova, O. Mukhametdinova, M. Markushev, *J. Alloy. Compd.* **746**, 520 (2018)
4. D.C.C. Magalhães, A.M. Kliauga, M.F. Hupalo, O.M. Cintho, C.A. Della Rovere, M. Ferrante, V.L. Sordi, *Mater. Sci. Eng. A* **768**, 138485 (2019)
5. Y. Zhang, S. Jin, P.W. Trimby, X. Liao, M.Y. Murashkin, R.Z. Valiev, J. Liu, J.M. Cairney, S.P. Ringer, G. Sha, *Acta Mater.* **162**, 19 (2019)
6. OSh. Sitdikov, E.V. Avtokratova, R.I. Babicheva, *Phys. Met. Metallogr.* **110**, 153 (2010)
7. A. Yamashita, D. Yamaguchi, Z. Horita, T.G. Langdon, *Mater. Sci. Eng. A* **287**, 100 (2000)
8. X. Sauvage, E.V. Bobruk, MYu. Murashkin, Y. Nasedkina, N.A. Enikeev, R.Z. Valiev, *Acta Mater.* **98**, 355 (2015)
9. X. Sauvage, M.Y. Murashkin, R.Z. Valiev, *Kovove Mater.* **49**, 11 (2011)
10. W. Xu, X.C. Liu, X.Y. Li, K. Lu, *Acta Mater.* **182**, 207 (2020)
11. H.J. Roven, M. Liu, J.C. Werenskiold, *Mater. Sci. Eng. A* **483**, 54 (2008)
12. M. Cabibbo, E. Santecchia, P. Mengucci, T. Bellezze, A. Viceré, *Mater. Sci. Eng. A* **716**, 107 (2018)
13. M.Y. Murashkin, I. Sabirov, A.E. Medvedev, N.A. Enikeev, W. Lefebvre, R.Z. Valiev, X. Sauvage, *Mater. Design* **90**, 433 (2016)
14. A. Mohammadi, N.A. Enikeev, MYu. Murashkin, M. Arita, K. Edalati, *Acta Mater.* **203**, 116503 (2021)
15. W. Chrominski, M. Kulczyk, M. Lewandowska, K.J. Kurzydowski, *Mater. Sci. Eng. A* **609**, 80 (2014)
16. A. Yousefi, A.R. Eivani, S.M.A. Boutorabi, H.R. Jafarian, *Mater. Sci. Eng. A* **713**, 180 (2018)
17. H. Yang, K. Li, Y. Bu, J. Wu, Y. Fang, L. Meng, J. Liu, H. Wang, *Scripta Mater.* **195**, 113741 (2021)
18. J.P. Hou, R. Li, Q. Wang, H.Y. Yu, Z.J. Zhang, Q.Y. Chen, H. Ma, X.M. Wu, X.W. Li, Z.F. Zhang, *J. Mater. Sci. Technol.* **35**, 742 (2019)
19. R.Z. Valiev, M.Y. Murashkin, I. Sabirov, *Scripta Mater.* **76**, 13 (2014)
20. K. Ma, H. Wen, T. Hu, T.D. Topping, D. Isheim, D.N. Seidman, E.J. Lavernia, J.M. Schoenung, *Acta Mater.* **62**, 141 (2014)
21. P. Frint, M.F.-X. Wagner, *Acta Mater.* **176**, 306 (2019)
22. Y. Iwahashi, Z. Horita, M. Nemoto, T.G. Langdon, *Acta Mater.* **45**, 4733 (1997)
23. W. Yang, M. Wang, R. Zhang, Q. Zhang, X. Sheng, *Scripta Mater.* **62**, 705 (2010)
24. S. Pogatscher, H. Antrekowitsch, H. Leitner, A.S. Sologubenko, P.J. Uggowitzer, *Scripta Mater.* **68**, 158 (2013)
25. W. Yang, L. Huang, R. Zhang, M. Wang, Z. Li, Y. Jia, R. Lei, X. Sheng, *J. Alloy. Compd.* **514**, 220 (2012)
26. W. Chrominski, M. Lewandowska, *Acta Mater.* **103**, 547 (2016)
27. W. Yang, S. Ji, L. Huang, X. Sheng, Z. Li, M. Wang, *Mater. Charact.* **94**, 170 (2014)
28. Y.W. Weng, Z.H. Jia, L.P. Ding, S.J. Muraishi, X.Z. Wu, Q. Liu, *J. Alloy. Compd.* **767**, 81 (2018)
29. M.H. Shaeri, M. Shaeri, M. Ebrahimi, M.T. Salehi, S.H. Seyyedein, *Prog. Nat. Sci.: Mater. Int.* **26**, 182 (2016)
30. G. Sha, K. Tugcu, X.Z. Liao, P.W. Trimby, M.Y. Murashkin, R.Z. Valiev, S.P. Ringer, *Acta Mater.* **63**, 169 (2014)
31. K. Majchrowicz, Z. Pakieła, W. Chrominski, M. Kulczyk, *Mater. Charact.* **135**, 104 (2019)
32. M.H. Mulazimoglu, R.A.L. Drew, J.E. Gruzelski, *J. Mater. Sci. Lett.* **8**, 297 (1989)
33. T. Hu, K. Ma, T.D. Topping, J.M. Schoenung, E.J. Lavernia, *Acta Mater.* **61**, 2163 (2013)
34. T. Huang, L. Shuai, A. Wakeel, G. Wu, N. Hansen, X. Huang, *Acta Mater.* **156**, 369 (2018)
35. O. Myhr, *Acta Mater.* **49**, 65 (2001)
36. D. Bardel, M. Perez, D. Nelias, A. Deschamps, C.R. Hutchinson, D. Maisonnette, T. Chaise, J. Garnier, F. Bourlier, *Acta Mater.* **62**, 129 (2014)
37. W. Guo, J. Su, W. Lu, C.H. Liebscher, C. Kirchlechner, Y. Ikeda, F. Körmann, X. Liu, Y. Xue, G. Dehm, *Acta Mater.* **185**, 45 (2020)
38. G.K. Williamson, W.H. Hall, *Acta Mater.* **1**, 22 (1953)
39. H. Wang, H. Geng, D. Zhou, K. Niitsu, O. Muránsky, D. Zhang, *Mater. Sci. Eng. A* **771**, 138613 (2020)
40. H. Asgharzadeh, A. Simchi, H.S. Kim, *Mater. Sci. Eng. A* **528**, 3981 (2011)
41. J.P. Hou, R. Li, Q. Wang, H.Y. Yu, Z.J. Zhang, Q.Y. Chen, H. Ma, X.M. Wu, X.W. Li, Z.F. Zhang, *J. Alloy. Compd.* **769**, 96 (2018)
42. N.D. Stepanov, A.V. Kuznetsov, G.A. Salishchev, G.I. Raab, R.Z. Valiev, *Mater. Sci. Eng. A* **554**, 105 (2012)
43. J.P. Hou, Q. Wang, Z.J. Zhang, Y.Z. Tian, X.M. Wu, H.J. Yang, X.W. Li, Z.F. Zhang, *Mater. Design* **132**, 148 (2017)
44. Z. Zhang, D.L. Chen, *Scripta Mater.* **54**, 1321 (2006)
45. Y. Harai, Y. Ito, Z. Horita, *Scripta Mater.* **58**, 469 (2008)
46. D. Setman, E. Schafner, E. Korznikova, M.J. Zehetbauer, *Mater. Sci. Eng. A* **493**, 116 (2008)
47. Y. Miyajima, S.-Y. Komatsu, M. Mitsuhara, S. Hata, H. Nakashima, N. Tsuji, *Philos. Mag.* **90**, 4475 (2010)
48. J. Čížek, M. Janeček, T. Vlasák, B. Smola, O. Melikhova, R.K. Islamgaliev, S.V. Dobatkin, *Mater. Trans.* **60**, 1533 (2019)
49. A.S. Karolik, A.A. Luhvich, *J. Phys.: Condens. Matter* **6**, 873 (1994)
50. G. Lin, Z. Zhang, H. Wang, K. Zhou, Y. Wei, *Mater. Sci. Eng. A* **650**, 210 (2016)

Publisher's Note Springer Nature remains neutral with regard to jurisdictional claims in published maps and institutional affiliations.